Analysis of Seasonal Current Variations in the Western Equatorial Indian Ocean: Direct Measurements and GFDL Model Comparison

MARTIN VISBECK AND FRIEDRICH SCHOTT

Institut für Meereskunde an der Universität Kiel, Kiel, Federal Republic of Germany

ABSTRACT

The seasonal cycles found in moored current measurements in the equatorial Somali Current region and along the equator between 50° and 60°E are compared with the multilayer Geophysical Fluid Dynamics Laboratory model for the tropical Indian Ocean. The remote forcing of Somali Current transport variations by incident long equatorial waves from the equatorial interior subthermocline region is investigated by analyzing the model velocities of annual and semiannual period. Amplitudes and phases of linear equatorial Rossby and Kelvin waves were least-squares fitted to the model velocities between 5°S and 5°N, 55° and 86°E from 100-m to 1000-m depth. Two cases of wave fits are distinguished: the "free" Kelvin wave case, where the Kelvin waves were fitted independently, and the "reflected" Kelvin wave case, where they were coupled to the Rossby waves by the western boundary condition for a straight slanted (45° to the north) coastline. The wave field velocities explained ~70% of the spatial variance in the equatorial model subregion and also compared reasonably well with observed current variations along the equator. At the western boundary, the short-wave alongshore transport due to reflected incident long waves was determined and found to be antisymmetric about the equator. The maximum transport variation for the semiannual period due to the short waves was about 5×10^6 m³ s⁻¹ between 150- and 800-m depth at 3° north and south of the equator. Observational evidence for the western boundary transport variations and the sensitivity to changes in the incident wave field are discussed.

1. Introduction

The western equatorial Indian Ocean is known for its drastic seasonal circulation changes in response to the annual cycle of the monsoon wind system. The interior equatorial region shows a dominant semiannual variation of zonal currents (Luyten and Roemmich 1982) that has been explained in terms of long equatorial waves, either vertically propagating (Luyten and Roemmich 1982; Wunsch 1977) or with standing vertical modes (Gent et al. 1983; Reverdin 1987). Although the response of the Somali Current to the onset of the summer monsoon has been fairly extensively studied in the Indian Ocean Experiment (INDEX, Leetmaa et al. 1982; Schott and Quadfasel 1982; Swallow et al. 1983), not much was known about its structure and annual cycle at the equator until recently. Moored array measurements on the equator show a striking asymmetry between both monsoon seasons (Schott 1986). While the Somali Current during the summer monsoon decays monotonically in the vertical, no deep-reaching boundary current exists during the winter monsoon. Instead, below the southwestward

surface flow, a northeastward countercurrent exists between about 150 and 400 m, followed again by weak southward current underneath, down to about the 1000-m level. This current structure does not appear to be continuous along the coast, but is confined to a narrow equatorial region that corresponds to the equatorial wave guide. At 5°N during the winter monsoon, the Somali Current flows southward, decaying monotonically in the vertical (Quadfasel and Schott 1983), and at 3°S the East African Coast Current, also decaying monotonically in the vertical, flows northward (Düing and Schott 1978).

The objective of this study is the analysis of the seasonal cycle in the western Indian Ocean along the equator and in particular its interaction with the western boundary, testing the hypothesis that the middepth variations of the equatorial Somali Current are at least partially related to "remote" forcing over the equatorial interior.

Lighthill (1969) first investigated the dynamic response of the Somali Current to westward-propagating Rossby waves, which were excited by an abrupt monsoon onset in the northern equatorial interior. He determined the remotely forced transport variations of the boundary current from incident Rossby waves without considering the reflected Kelvin waves. A more general form of low-frequency equatorial wave reflection at arbitrary western boundaries, which includes

Corresponding author address: Dr. Martin Visbeck, Institut für Meereskunde an der Universität Kiel, Düsternbrooker Weg 20, D-2300 Kiel 1, Federal Republic of Germany.

the Kelvin waves, is given by Cane and Gent (1984) and will be applied here.

Because of the paucity of observations from that region, the principle analysis will be made on the multilayer Geophysical Fluid Dynamics Laboratory (GFDL) model after it is determined that this model agrees qualitatively well with the overall observational evidence in the western Indian Ocean.

Observations used will be moored current measurements by Luyten and Roemmich (1982) taken over a 15-month period in the depth range 200–750 m at several points along the equator and moored current measurements taken over a 2-year period in the Somali Current on the equator between 50 m and 1000 m by Schott et al. (1990).

The basic features of the GFDL primitive equation model of G. Philander are described by Philander and Pacanowski (1986) for an application to the tropical Atlantic. The model is forced by the seasonally varying climatological wind-stress fields of Hellerman and Rosenstein (1983).

After a summary of the pertinent observations used and a brief review of the model output fields and comparison with observations, we will decompose the observed and model currents into Fourier harmonics and find that most of the variance can be explained by the annual plus semiannual period, though with significantly different contributions along the equator in the interior and at the western boundary.

We will then fit long equatorial waves to the GFDL model velocity harmonics within an equatorial subthermocline region using a standard least-squares technique. The western boundary response to incident long waves will be investigated by assuming that the Kelvin waves match the boundary-reflected Rossby waves. The resulting short-wave transport will be found to play a key role in remotely forcing the Somali Current below 150-m depth. A sensitivity study of the short-wave transport to different subsets of incident long waves is included.

2. Moored current measurements

An array of moored current meters was deployed by the Woods Hole Oceanographic Institution Buoy Group in April 1979 and recovered in June 1980 as a component of the Indian Ocean Experiment (INDEX). The array spanned 12° of longitude along the equator, from 47° to 59°E (Fig. 1a,b). The six equatorial moorings had nominal instrument depths of 200, 500, and 750 m, and the current records were kindly made available by J. R. Luyten. The zonal velocities in the 50°–60°E longitude range show a coherent seasonal signal of dominantly semiannual nature in each layer as shown for all 750-m depth records (Fig. 2a; Luyten and Roemmich 1982).

Two phases of enhanced eastward wind stress over the central equatorial Indian Ocean during the course
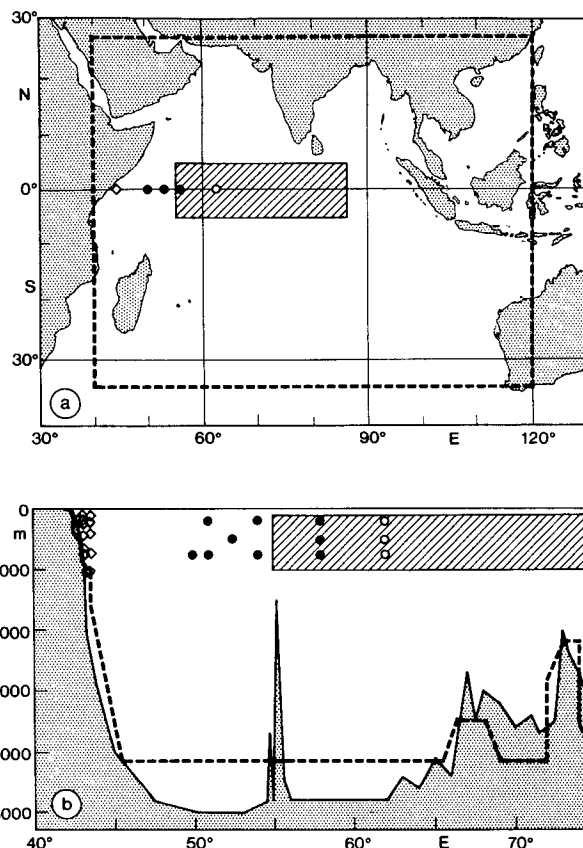

FIG. 1. (a) Map of the Indian Ocean including the Somali Current moorings (◇), the INDEX moorings (●, O), the subregion for the wave fit to the model (shaded), and the GFDL model domain (dashed). (b) Section along the equatorial Indian Ocean. The shaded area is the subregion used for the wave fit, and the dashed line indicates the GFDL model topography.

of the year, in May and October, force a strong equatorial surface jet of semiannual period (Wyrtki 1973). This is shown for the Hellerman and Rosenstein (1983) wind stress at 65°E, for two boxes between 0°–2°N and 0°–2°S (Fig. 2b). The corresponding observed ship drift velocities (Fig. 2c; Cutler and Swallow 1984) are eastward at about 60 cm s⁻¹ and in phase with the wind-stress variations, while the flow at 750-m depth shows ~180° phase difference and about 25 cm s⁻¹ amplitude. This vertical flow structure is in agreement with the second baroclinic mode: The surface velocities are directed opposite to the velocities below 200 m, and the amplitudes at the 750-m level are about one-third of the surface value. It is noteworthy that the "local" wind stress (with respect to the mooring locations) at 55°E shows a dominant annual signal and only weak semiannual variations compared to the wind stress at 65°E (Fig. 2b). This suggests that the observed semiannual current variations between 50° and 60°E may be remotely forced farther east.

Two consecutive arrays of moored current meters
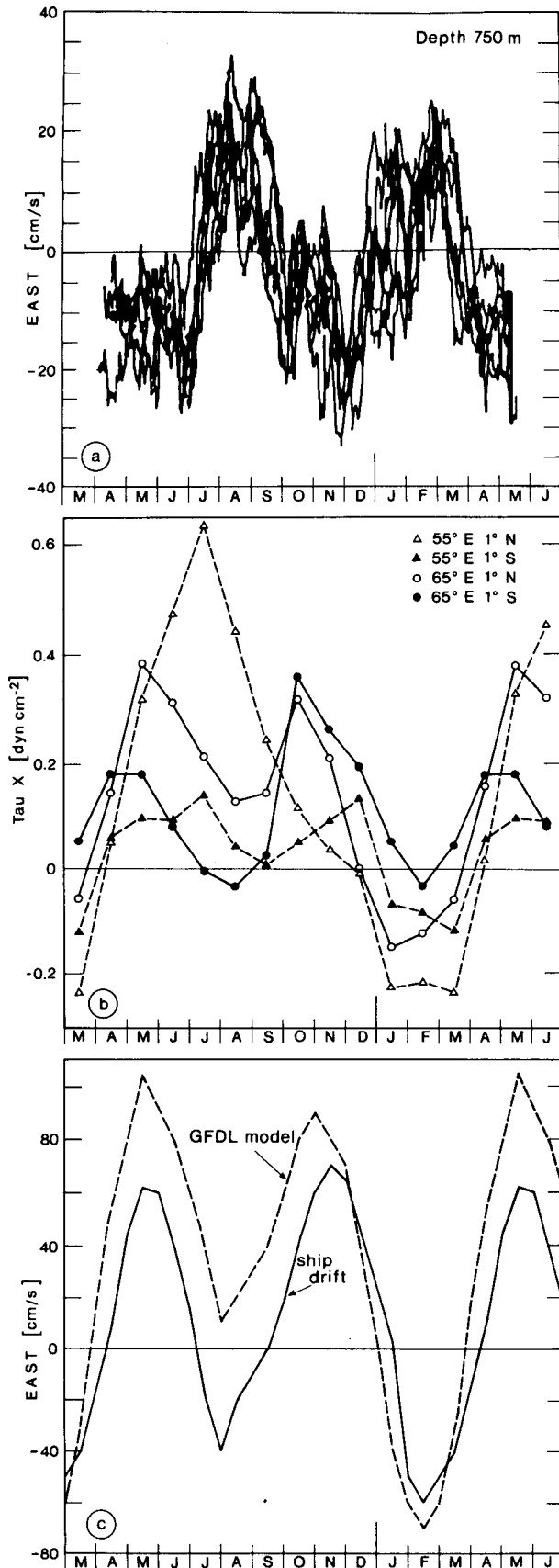
were deployed in the Somali Current during October 1984–September 1985 and September 1985–October 1986. The moorings spanned the region of the western boundary current between 43° and 44.5°E along the equator. The observations of the first year were described and compared with GFDL model results by Schott (1986) under the aspect of the seasonally varying vertical structure of the Somali Current. Seasonal means and transports were presented by Schott et al. (1990). Figure 3a shows vector plots of the FSU ship observed wind velocities (J. Legler, personal communication) representing the annual reversal of the monsoon wind system that is mainly parallel to the coastline with typical values of 10 m s^{-1}. The current meter velocity vectors (Fig. 3b) split into three essentially different layers for the equatorial Somali Current. (i) The upper 150 m show a "local" monsoon forced behavior with southwestward flow during the northeast monsoon and northeastward flow during the southwest monsoon in late summer and velocities in the order of 1 m s^{-1}. (ii) Between 150 and 300 m the monsoon correlated signal gets weaker, and a mean flow of about 20–50 cm s^{-1} dominates the flow. The mean northeastward velocity reverses for only about two months in late spring and is somewhat different in both years. (iii) Below 300 m, smaller seasonal variations are found and the main current reversals consist of about a two-month period.

Part of the middepth variations might be remotely forced by equatorial waves; they will be investigated in the following section using the GFDL model data. Unfortunately, it will be found that right at the equator the alongshore wave–induced transport changes very rapidly with latitude making the comparison with the equatorial mooring data from the western boundary less helpful than anticipated.

3. GFDL numerical model

We have analyzed the output fields of the three-dimensional primitive equation model run by G. Philander at GFDL in Princeton. The model domain is the tropical Indian Ocean north of 34°S and west of 120°E (Fig. 1a). The 104 zonal grid points have the best resolution of 0.5° west of 60°E decreasing to 1° east of 70°E. The 96 meridional grid points resolve 0.3° between 5°S and 15°N, and the spacing increases toward high latitudes. The vertical resolution of the 27 layers is 10 m for the top 100 m and increases gradually to 600 m for the lowest layer (3800 m). The model temperature and salinity are relaxed to the monthly

FIG. 2. (a) Time series of zonal velocity from seven instruments at 750-m depth close to the equator between 50° and 60°E (from Luyten and Roemmich 1982). (b) Hellerman and Rosenstein (1983) zonal wind stress for 55°E at 1°S and 1°N and for 65°E at 1°S and 1°N. (c) Surface zonal velocity averaged between 1°S and 1°N at 65°E for ship drifts (solid) and GFDL model (dashed).
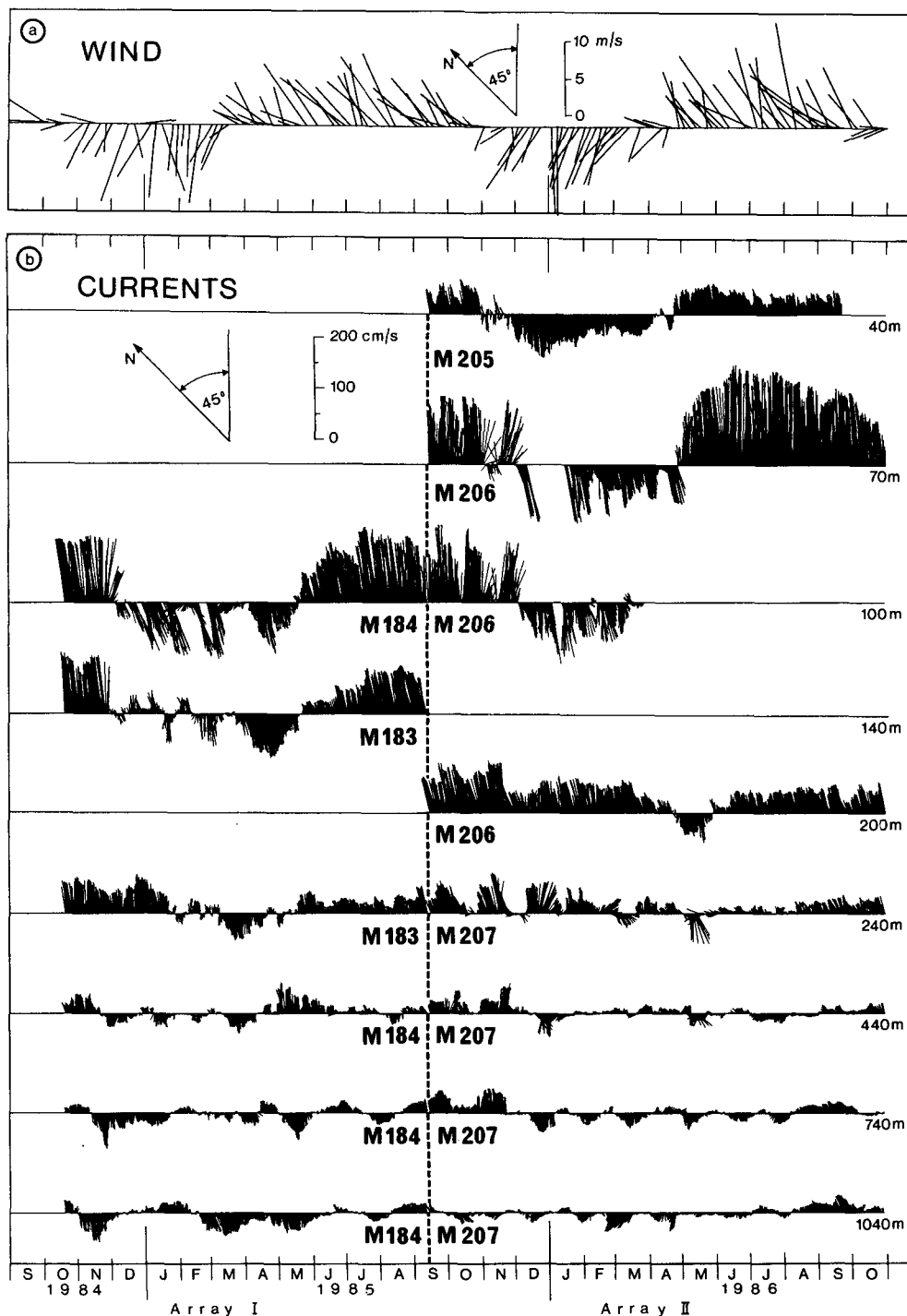
FIG. 3. (a) Vector plots of FSU ship-observed wind velocities (upward is parallel to coast, toward northeast). (b) Vector plots of 40-h low-pass Lanczos filtered currents (upward is parallel to coast) for two years of deployment in the Somali Current on the equator. Station M183/M206 are 2 miles off the shelf, and M184 is 12 miles and M207 is 26 miles eastward from the shelf.

mean climatological values of Levitus (1982) southward of 20°S, and there are no open boundaries. The model configuration and parameters are the same as for the tropical Atlantic Ocean model (Philander and Pacanowski 1986). At the surface the model temperature is determined by a climatological heat flux con-

dition while no condition is applied to salinity. The model has been forced by the climatological wind stress of Hellerman and Rosenstein (1983) and run for 3 years. The last year was investigated here using monthly instantaneous data fields containing U, V, W, T, and S at each grid point.

The GFDL model fields for the Indian Ocean have not yet been fully investigated, except for some comparison work at the equator (Schott 1986) and in the southwestern subtropical Indian Ocean (Schott et al. 1988), which is briefly summarized as follows. At the western boundary on the equator, model and observed current profiles compare reasonably well and will be investigated here in more detail. The comparison in the southwestern Indian Ocean showed too weak annual mean model transports: (i) for the current past the northern tip of Madagascar, observations lead to a transport of 30 Sv (Sv = 10^6 m^3 s^{-1}) in the upper 1000 m, compared to only about 3 Sv for the model; (ii) the South Equatorial Current is too weak, with 22 Sv for the total model transport at 54°E between 11° and 23°S compared to 40 Sv for the geostrophic transport from observations.

To investigate the western boundary response of long waves we found that the velocity observations of Luyten and Roemmich (1982) were not sufficient to resolve the different long-wave modes because of the small zonal array extent of ~10°. Therefore we analyzed the GFDL model fields and will include a comparison of model velocities with observations in the western equatorial Indian Ocean to justify the use of the GFDL model for the wave analysis.

a. Equatorial surface velocities

The seasonal cycle of the model surface zonal velocity is compared with ship drift data (Reverdin 1987; Cutler and Swallow 1984). The observed and model datasets are averaged between 1°S and 1°N on a monthly basis. The equatorial jet is the dominant observed signal (Fig. 4a) with two three-month long periods of eastward velocity (80 cm s^{-1} maximum) and weaker westward flow in between. The corresponding model surface currents show a more asymmetric variation during the course of the year (Fig. 4b) with maximum eastward flow in May (120 cm s^{-1}) being larger than in October (80 cm s^{-1}) and no westward reversal in between. This appears as an amplified annual signal in the harmonic analysis.

b. Equatorial undercurrent

The equatorial undercurrent has been extensively studied in the Pacific and Atlantic oceans, but only sparse observations exist in the Indian Ocean. From what is known the undercurrent exists only in spring (Leetmaa and Stommel 1980; Taft and Knauss 1967).
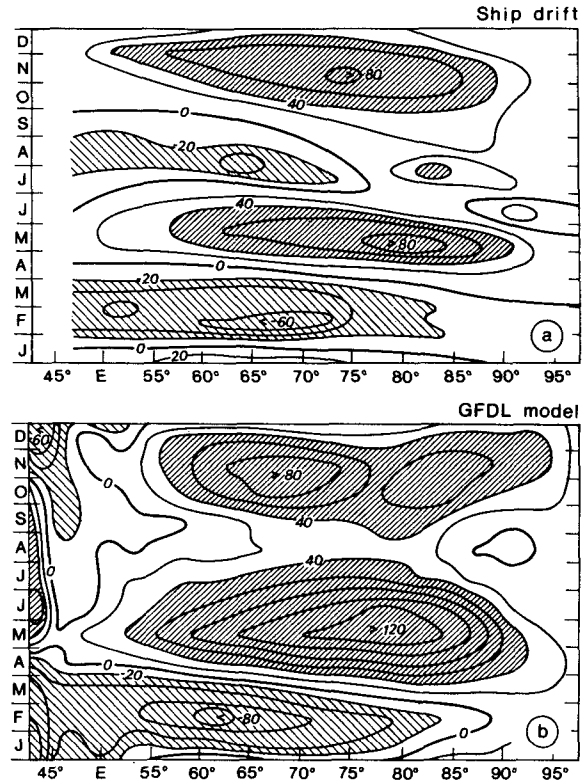

FIG. 4. Zonal velocities in the equatorial band, averaged between 1°S and 1°N: (a) ship drift currents (from Reverdin 1987), (b) surface-layer currents from the GFDL model.

A subsample of meridional sections of zonal velocity at 53°E from Leetmaa and Stommel (1980) is compared with the model currents (Figs. 5a,b). From all observations the closest dates to the 15th of each month have been selected. In February and March the model represents the observed undercurrent with a core depth of 70 m, but the maximum model velocity (50 cm s^{-1}) is weaker than the observed (60–80 cm s^{-1}). Later in the season, the undercurrent decays and merges with the South Equatorial Current with good agreement between model and observation. The East Monsoon Current is too weak in the model and almost disappears in April.

The model undercurrent along the equator (Fig. 5c) shows the typical shallowing of the core depth from west to east only in the western part of the basin (west of 60°E). In the central Indian Ocean, east of 60°E, the model undercurrent shows a larger vertical extent with weaker velocities compared to the western branch. The only available observations from the eastern basin (Taft and Knauss 1967) at 92°E show a velocity maximum of 60 cm s^{-1} at about 110-m depth, in qualitative agreement with the model.

In summary, the GFDL model reproduces the undercurrent during the appropriate time of the year but with weaker peak velocities than observed.
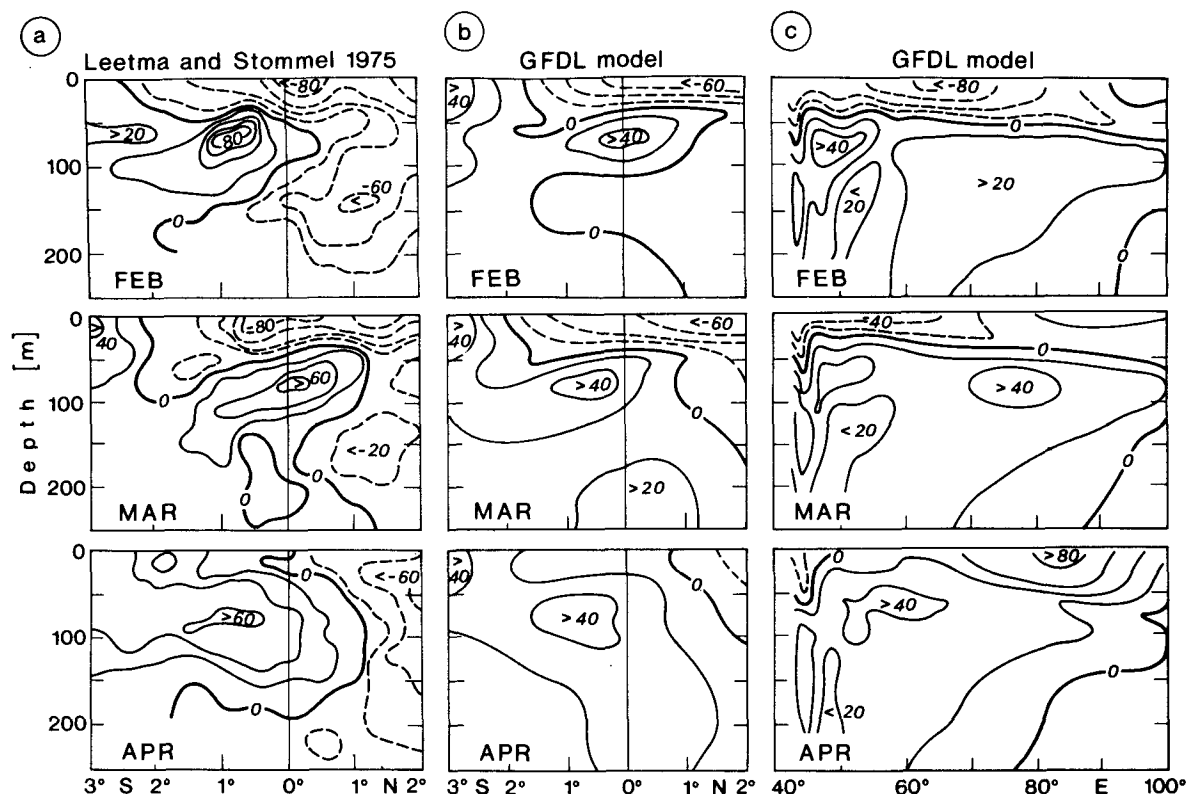
FIG. 5. Meridional section along 53°E of zonal velocities: (a) Observations (from Leetmaa and Stommel 1976) and (b) GFDL model results. (c) Zonal section along the equator of GFDL model zonal velocity. Westward velocities are dashed.

c. Deep equatorial jets

Deep equatorial currents where observed by a free-falling current profiler (White Horse) along the equator between 47° and 62°E (Luyten and Swallow 1976; Ponte and Luyten 1990). Energetic zonal velocity variations were found on vertical scales of approximately 100 m modifying the current reversals that occur on a larger vertical scale (Fig. 6a, from Ponte and Luyten 1990). The corresponding model profiles (Fig. 6b) show indications of only the larger-scale reversals with westward flow between 200 and 1500-m depth below the eastward surface jet. The small-scale variations are not present in the model fields, probably due to the coarse vertical resolution in the model below the thermocline.

In general, some of the observed reversals with a vertical scale in the order of 1000 m appear to be represented by the model, but there is no significant flow below 1500-m depth in the model. Because of this obvious deficiency of the deep model velocities we restricted the following analysis to the upper 1000 m.

4. Analysis

a. Harmonic analysis

Two periods are dominant in the observations and model velocities: the annual and semiannual. To sep-

arate the velocity variations for each period, the time series were subjected to harmonic analysis. The relative importance of the harmonic energy is given by the resolved variance: the ratio of total variance minus residuum variance to the total variance or the squared correlation coefficient.

The annual amplitude, phase, and resolved variance of the GFDL model zonal velocities along the equator is shown in Fig. 7a. The vertical axis is transformed to equal increments of $\int N dz$ for a mean model N (stability) profile to enlarge the thermocline region. The largest energy is found in the upper layer of the Somali Current with amplitudes of more than 80 cm s^{-1} and a second maximum at 50°E in about 75-m depth, representing the annual variation of the western Equatorial Undercurrent. At the surface between 60° and 80°E the annual harmonic of the equatorial jet variation gives amplitudes of 20 cm s^{-1}, but there the resolved variance is small, therefore indicating that the main energy is not of annual period. The phase increases upward and westward for a broad interior region below 200-m depth. Small vertical phase changes separate the western boundary regime from the interior near 47°E. The explained variance gives high values (>80%) for the upper Somali Current region and reasonable values in the undercurrent layer.

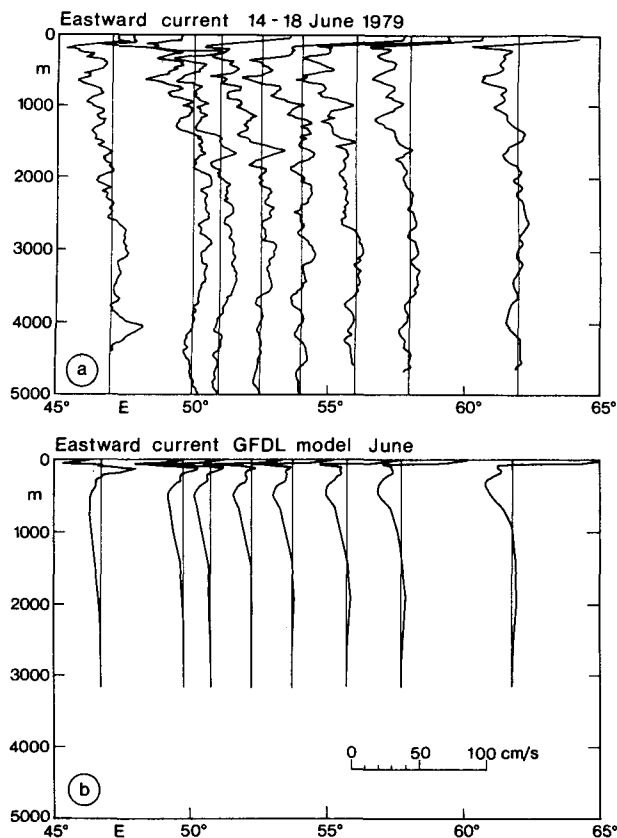The semiannual signal (Fig. 7b) shows the largest

FIG. 6. Zonal velocity profiles along the equator in June: (a) White Horse observations (from Ponte and Luyten 1990) and (b) corresponding GFDL model profiles.

amplitudes for the equatorial jet with maximum 60 cm s^{-1} at the surface and explains more than 60% of the monthly variance. Again, the phase increases upward and westward below the thermocline, but for the semiannual period the western boundary matches the interior with a similar vertical phase structure. The resolved variance indicates that the model variations below the thermocline are mainly of semiannual period west of 85°E with amplitudes in the order of 10 cm s^{-1}.

The observed semiannual zonal velocities (Luyten and Roemmich 1982) show somewhat larger amplitudes at the mooring locations than the model (Table 1). The observed eastward phase propagation in the 205-m layer west of 58°E is not present in the model, but below, the model phases agree within 20° with the observations.

The semiannual plus annual GFDL model harmonics explain more than 90% of the monthly zonal velocity variance in the subthermocline interior region along the equator (not shown), therefore, the following analysis is restricted to these periods.

Some of the western boundary signal of the zonal velocity was mentioned earlier in this section. Now we

compare the alongshore (45 degree rotated) velocities of the model with current meter observations for an average equatorial Somali Current profile. Figure 8 shows profiles of the mean flow and amplitudes of annual and semiannual variations. The model profiles were averaged between 43° and 44°E, and current meter observations (Schott 1986) were averaged for both years in six vertical layers. In the upper 100 m the main energy is of annual period with velocity amplitudes between 50 and 150 cm s^{-1}. The model profile of annual amplitudes decays more rapidly than the observations, which show significant variations between individual measurements (error bars). The semiannual variations are small, and the mean flow is directed northward with about 40 cm s^{-1} in the upper layer. Between 150 and 300-m depth, the model mean flow has larger velocities ($\sim$50 cm s^{-1}) than the observed mean of about 25 cm s^{-1} and dominates the annual and semiannual variations. Below 300 m, both the annual and semiannual periods contribute to the velocity variations with slightly weaker model amplitudes in the order of 10 cm s^{-1}.

In general, only the main features of the equatorial Somali Current compare qualitatively well between the model and observations.

So far, we have investigated the vertical variations at the equator, and to show the horizontal variations, the harmonic amplitudes between 5°S and 5°N for the western Indian Ocean are displayed as current vector ellipses (similar to tidal ellipses) for three model layers (Fig. 9): The upper (15-m depth) layer shows significant annual energy north of the equator representing the variations of the southern extent of the Monsoon Current at 5°N and at the western boundary, the Somali Current reversal appears on a 150-km wide band with annual alongshore amplitudes of $\sim$100 cm s^{-1}. The semiannual amplitudes show equatorially trapped current oscillations of $\sim$75 cm s^{-1} zonal amplitude in the interior region (equatorial jet). At 205-m depth both periods show equal amplitudes ($\sim$15 cm s^{-1}) along the equator, and the western boundary region is separated from the interior at about 50°E. Farther down, at 483-m depth the energy decreases, but the equatorial band of relatively high energy reaches closer to the western boundary. The annual harmonic Somali Current variations are enhanced north of the equator (15 cm s^{-1} at 3°N) connecting the equatorial band with the Monsoon Current stretching eastward north of 5°N. The semiannual variations of the Somali Current at intermediate depth are rather symmetric along the boundary separating into a northern and southern branch with a minimum inbetween close to the equator (Fig. 9b lower panel). It is this structure that we will find to be remotely forced by long waves.

Overall, the GFDL model harmonic velocities show equatorial "trapped" energy for both periods below the thermocline. One way of interpreting the meridional trapping scale ($\sim$3°) and the upward and westward
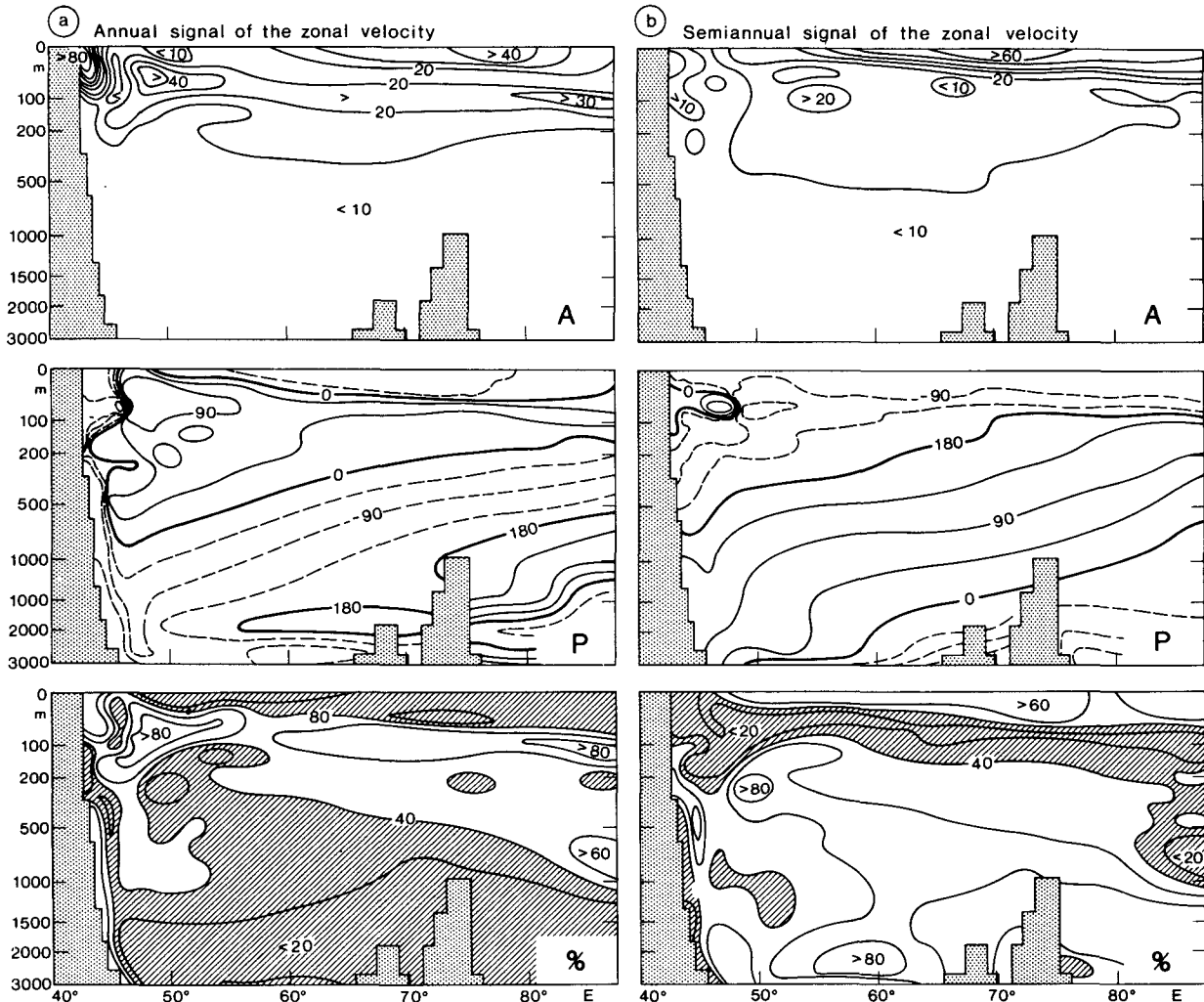
FIG. 7. Zonal section along the equator of the GFDL model zonal velocity. Vertical axis is transformed to equal $\int Ndz$ using a mean N (stability) profile. Amplitudes (A, top), phases relative to the 1 January (P, middle), and the explained variance (%, lower) for (a) the annual harmonic and (b) the semiannual harmonic.

phase propagation of the zonal velocity along the equator is by assuming the presence of long equatorial waves. The latter will be determined by the wave fit.

b. Long equatorial waves

Luyten and Roemmich (1982) analyzed zonal velocity variations along their mooring array. They explained the observed amplitudes and phases of semiannual period by vertically propagating long waves. The comparison between the theoretical and observed ratio of zonal to vertical phase speeds plus the ratio of potential to kinetic energy led them to an interpretation by a superposition of a Kelvin and Rossby wave mode.

A different approach by Gent et al. (1983) explained the same observations by a linear equatorial wave model with vertically standing modes forced by the semiannual component of the zonal Hellerman and

Rosenstein (1983) wind-stress climatology. The zonal velocities of the over 100 forced Rossby and Kelvin waves explained the westward and upward phase propagation to a good extent, but their model wave amplitudes were smaller than the observations.

In contrast to Gent et al. we have determined the wave energy for each wave mode by fitting linear unforced waves to the GFDL model velocity harmonics rather than projecting the wind energy on to vertical modes.

First, an unforced equatorial wave model was set up (Appendix Eq. (A1); e.g., Moore and Philander 1977) and the vertical problem was separated by normal baroclinic modes, using a mean N (stability) profile out of the GFDL model (Fig. 10a) that yielded slightly smaller equivalent depths (Table 2) than those derived from observed CTD profiles for May and June 1976 at 53°E (e.g., Gent et al. 1983).

TABLE 1. Amplitude (cm s^{-1}) and phase (relative to 1 January) of the semiannual zonal velocity harmonic at four longitudes along the equator.

Depth (m)	Longitude (E)			
	50° or 51°	54°	58°	62°
	Observations: Luyten and Roemmich (1982)			
200	15.0 (161°)	18.0 (170°)	17.0 (194°)	14.0 (164°)
500	10.0 (142°)	—	15.0 (136°)	18.0 (122°)
750	14.0 (115°)	14.0 (97°)	14.0 (107°)	9.0 (92°)
	Wave model Gent et al. (1983)			
200	10.8 (187°)	9.9 (174°)	10.0 (147°)	6.9 (170°)
500	7.8 (136°)	7.9 (119°)	8.8 (106°)	10.0 (96°)
750	6.0 (128°)	6.3 (113°)	7.8 (103°)	11.2 (91°)
	GFDL model			
205	14.8 (230°)	12.1 (215°)	12.4 (198°)	12.8 (181°)
483	8.3 (150°)	9.3 (143°)	10.6 (135°)	10.3 (129°)
680	6.3 (121°)	7.3 (109°)	8.4 (100°)	7.8 (95°)
	Wave fit to GFDL model, free Kelvin wave case			
200	10.9 (214°)	11.7 (203°)	11.4 (193°)	10.4 (184°)
500	5.2 (160°)	5.9 (147°)	6.9 (135°)	6.9 (117°)
750	4.5 (135°)	5.4 (121°)	6.5 (109°)	7.3 (91°)
	Wave fit to GFDL model, reflected Kelvin wave case			
200	10.8 (237°)	11.4 (217°)	11.6 (201°)	11.2 (188°)
500	5.6 (182°)	6.2 (164°)	7.2 (146°)	6.9 (125°)
750	5.2 (135°)	5.8 (122°)	6.9 (108°)	7.5 (86°)

Projecting the semiannual harmonics of a zonal GFDL velocity profile at 53°E on the equator into baroclinic modes shows that most of the energy is rep-resented by the first three baroclinic modes (Fig. 10b). It is noteworthy that the mode energies compare well with the mode amplitudes of Gent et al. (1983), since they used the projection of the semiannual wind-stress harmonic to calculate their modal forcing amplitudes.

A subsample of the equatorial GFDL model grid points was used to fit the amplitudes and phases of long waves to the zonal and meridional velocity harmonics. Twelve unforced waves were used for the fit, consisting of four waves for each of the first three baroclinic modes, namely, the first three meridional modes of long Rossby waves and the Kelvin wave. The fit uses a standard least-squares technique for overdetermined problems assuming uncorrelated data with 1 cm s^{-1} error and no a priori information.

The standard case region is a box between 5°S and 5°N, 55° and 86°E and 100–1000-m depth. The spacing was determined by the first minimum of the zonal–meridional cross-correlation function that was found to be approximately 1° in meridional and 6° in zonal direction. With eight depth layers used in the fit, this yielded 384 grid points of which 70 (subsampled by a factor of 5.5 in longitude, latitude, and depth) were used for the fit within the equatorial subthermocline box.

The energy and phase, which is relative to the western boundary and 1 January, resulting from the fit for each of the 12 waves, is shown in Fig. 11 for the annual and semiannual periods (thin lines). A second class of solutions was found by assuming the Kelvin waves to be excited by the reflection of the long Rossby waves off the western boundary for each vertical mode. The boundary condition used here is that of Cane and Gent (1984) for a straight coastline at 45° inclination against north [Appendix Eq. (A2)], which implies that away
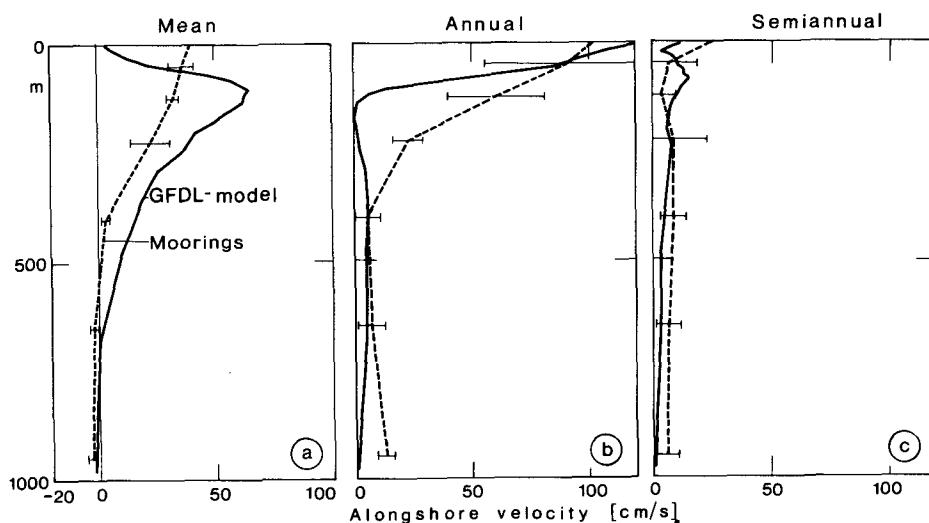

FIG. 8. Somali Current alongshore profiles (45° rotated) at the equator of the GFDL model (solid lines), averaged between 43° and 44°E, and the observations, averaged for six layers of both deployment years (dashed lines) including standard deviations among the instruments (errorbars) for (a) the mean flow, (b) the annual harmonic, and (c) the semiannual harmonic amplitude.
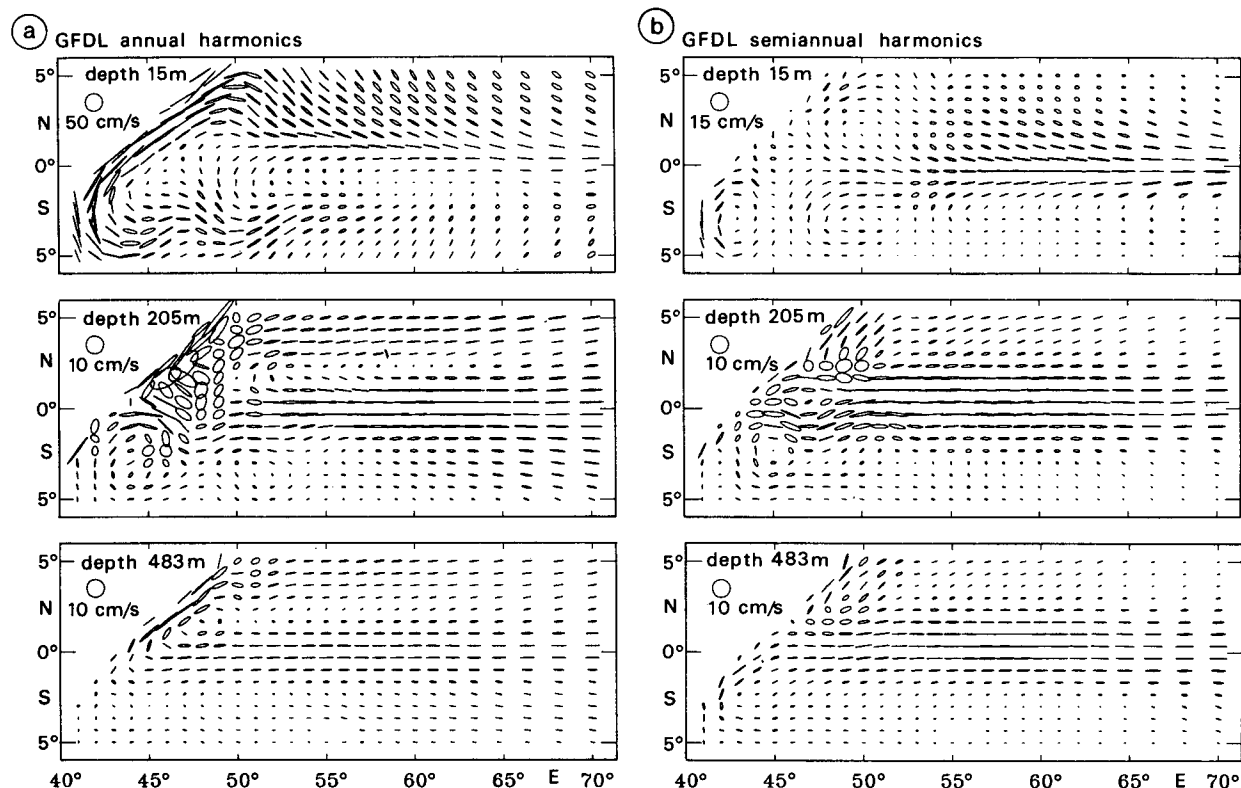
FIG. 9. Horizontal velocity ellipses of the GFDL model at 15-m, 205-m, and 483-m depth for (a) the annual and
(b) the semiannual period. Each second GFDL model grid point is displayed.

from the boundary only Kelvin and long Rossby waves remain. The results (Fig. 11, thick lines) are fairly different from fitting "free" Kelvin waves: the energy is

distributed differently between the Kelvin and the first-meridional-mode Rossby wave (hereafter Rossby 1 wave). Generally, the Rossby 1 wave of the first and second baroclinic mode contains the largest fraction of the total energy, but the other wave modes cannot be neglected. Only the wave energies of the third baroclinic mode are significantly smaller.

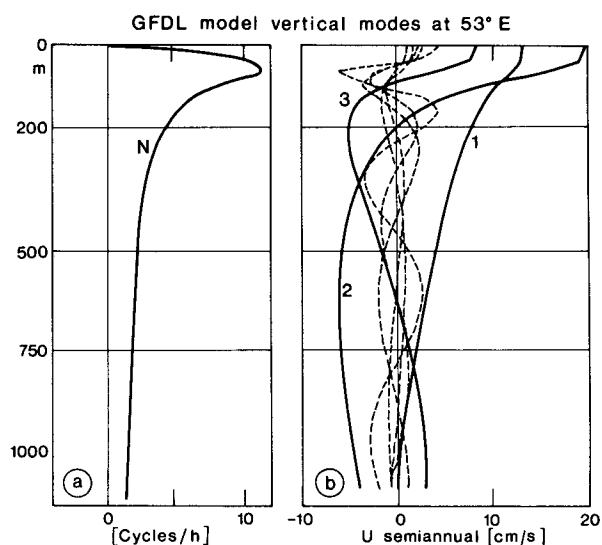Figures 12a,b display the annual and semiannual

FIG. 10. (a) Stability (N) for a mean GFDL model density profile. (b) First eight normal modes multiplied by the mode amplitudes found for a GFDL semiannual harmonic zonal velocity profile at 53°E on the equator.

TABLE 2. Vertical mode parameter: equivalent depth (h), Kelvin wave phase speed (c), and length scale (r) for a mean equatorial GFDL model N (stability) profile. Equivalent depth (h_{CTD}) for an average CTD stability profile during May and June 1976 at 53°E at the equator and the projection coefficient (P_r) for the semiannual Hellerman and Rosenstein (1983) zonal wind-stress component (Gent et al. 1983).

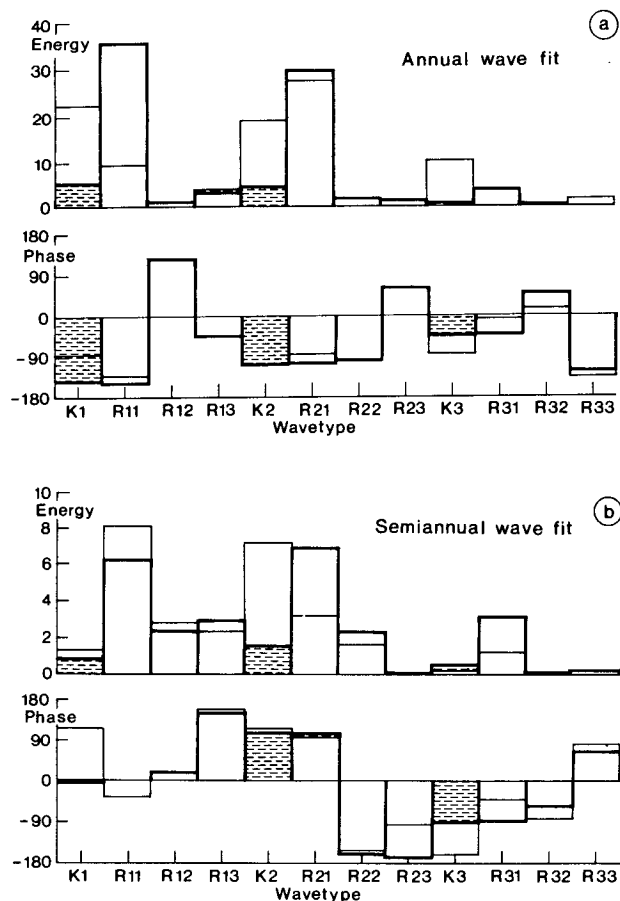|	Vertical mode number			
	1	2	3	4
	GFDL model			
h (cm)	63.6	22.2	9.9	5.5
c (cm s^{-1})	250	148	99	73
r (km)	330	253	207	178
	CTD observations			
h_{CTD} (cm)	79.9	30.5	12.6	6.5
P_r	3.9	5.5	2.5	2.1

FIG. 11. Energy (cm² s⁻²) and phases (degree, relative to the 1 January and 42.5°E) of the long equatorial Rossby waves (Rnm) fitted to the GFDL model velocities plus the appropriate Kelvin (Kn) waves for (a) the annual and (b) the semiannual period. Thick lines represent the reflected Kelvin wave fit with the Kelvin waves (shaded) being depended from the Rossby waves. Thin lines represent the independent free Kelvin wave fit.

harmonics of the sum of all long waves from the fit ("reflected" Kelvin wave case). The horizontal distribution of the long-wave energy at 480-m depth shows the equatorial band of maximum variance and should be in agreement with the GFDL harmonics (Figs. 9a,b, lower panels). The residual amplitudes between model and waves fitted to the model are shown in Figs. 12c,d, with the annual period showing the largest differences (>10 cm s⁻¹) in the western boundary region, while the equatorial residual amplitudes are small (2–3 cm s⁻¹). The semiannual residuum shows a region of misfit beginning at the equator at 47°E and stretching eastward along 1°S (Fig. 12d). The western boundary misfit for the long waves is confined to a band of 2° width, where it has to be noted that the short-wave contribution at the boundary is not included.

Nevertheless, the wave fit reproduces most of the spatial variance of the GFDL model harmonics with a correlation of 0.82 throughout the subgrid for both

periods for the reflected Kelvin wave fit and 0.87 for the free Kelvin wave case. This appears to be sufficient for studying the associated western boundary response.

c. Waves at the western boundary

The interaction of the waves at the western boundary with the Somali Current is governed by the short Rossby and Yanai waves. Although the short waves have not been computed explicitly by the fit, their integral transport can be calculated by making use of two features [Appendix Eq. (A3); e.g., Cane and Sarachik 1977]. (i) The transport can be expressed by a stream-function because the velocities are almost nondivergent. (ii) The slow eastward group speed traps the short waves to the western boundary region for only a small amount of friction. The zonal scale of the short-wave-induced boundary current is independent of the vertical and meridional modal structure and only a function of frequency [dispersion relation, see Appendix Eq. (A3)] giving 55 km for the annual and 110 km for the semiannual period. The smaller of these scales is of the same order as the zonal resolution of the GFDL model (0.5°) and the typical mooring distance for the Somali Current array. We are aware of possible model resolution problems, but there was only one model run available, and therefore, the role of resolution could not be investigated in any detail. However, as Veronis (1965) points out for a wind-driven boundary current, a model distributes the small-scale (relative to the grid size) behavior of a physical system (and its accompanying effects) throughout the domain, for example, the regime where boundary current variations occur can expand into the ocean interior. With the boundary scale barely resolved, we expect at least the integral effect of the short waves (e.g., transport) to be properly represented.

The incident long waves used to determine the short-wave transport were those of the reflected Kelvin wave fit, since they solve the western boundary condition by definition. The resulting short-wave alongshore transport for the sum of the annual and the semiannual period is displayed in a latitude versus time diagram for 483-m depth (Fig. 13a). The transport is antisymmetrical to the equator with southwestward transport of 15×10^3 m³ s⁻¹ per meter depth at 2.5°N and a northeastward transport of the same order at 2°S in April. This convergence at the equator changes to a divergence for the next four months. Then, between October and January the transports are weaker and a northeastward flow of 5×10^3 m² s⁻¹ exists at the equator. For comparison, the GFDL model alongshore velocity harmonics were integrated along a 200-km (4 grid points) long section normal to the western boundary and are displayed in the same fashion for the same depth (Fig. 13b). The transport (per meter depth) variations show a similar antisymmetric pattern during the course of the year as the transports of the short waves. But the GFDL model northeastward flow between July

Wave fit annual harmonics
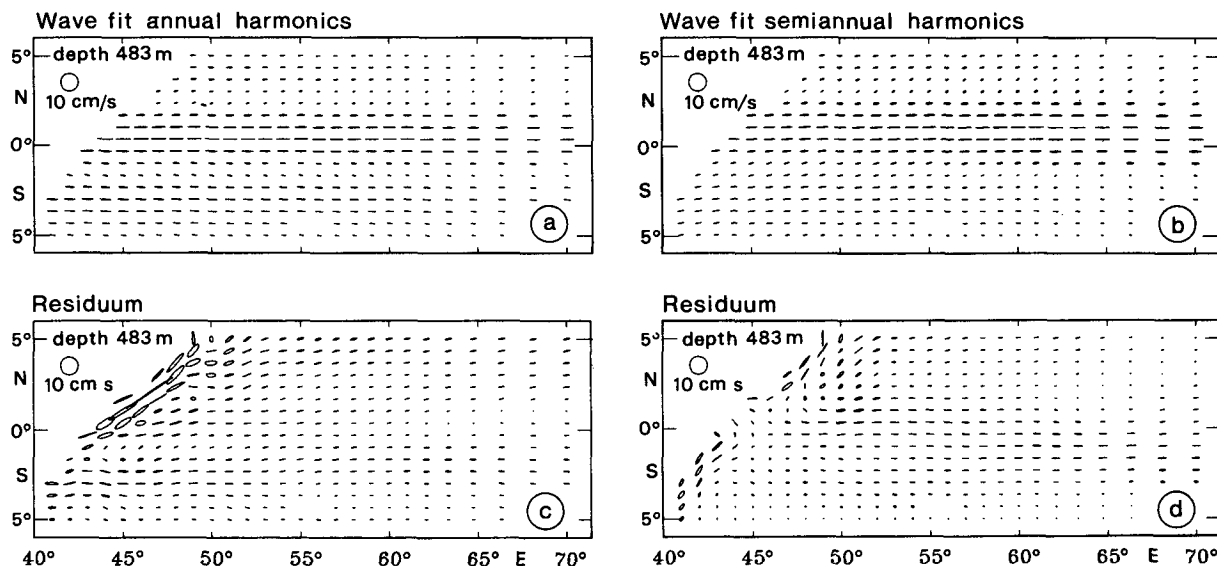
Wave fit semiannual harmonics

FIG. 12. Horizontal velocity ellipses at 483-m depth for the long waves of the reflected Kelvin wave fit for (a) the annual and (b) the semiannual period. Residuum ellipses for the (c) annual and (d) semiannual period.

and October seems to propagate southward rather than to show the abrupt phase change predicted by the waves.

This antisymmetrical boundary current structure of the short-wave transports with respect to the equator

shows large meridional gradients close to the equator. Unfortunately the mooring array was located in that region of rapidly changing transports, and small meridional shifts of the wave pattern due to mean-flow interaction, coastline geometry, bathymetry, etc., can
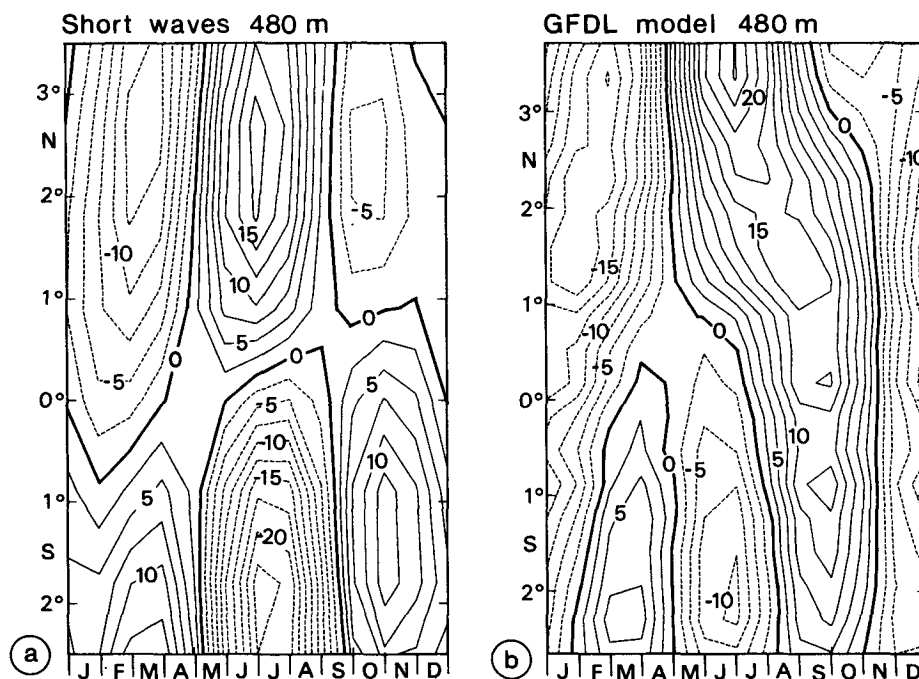
Short waves 480 m

GFDL model 480 m

FIG. 13. Western boundary current transport per meter depth (10^3 m^2 s^{-1}) as a function of time and latitude for 483-m depth of (a) the short waves resulting from long-wave reflection (reflected Kelvin wave fit) and (b) the GFDL model, averaged along sections normal to the western boundary of $\sim2°$ length. Northeastward transport contours are solid, southwestward dashed.
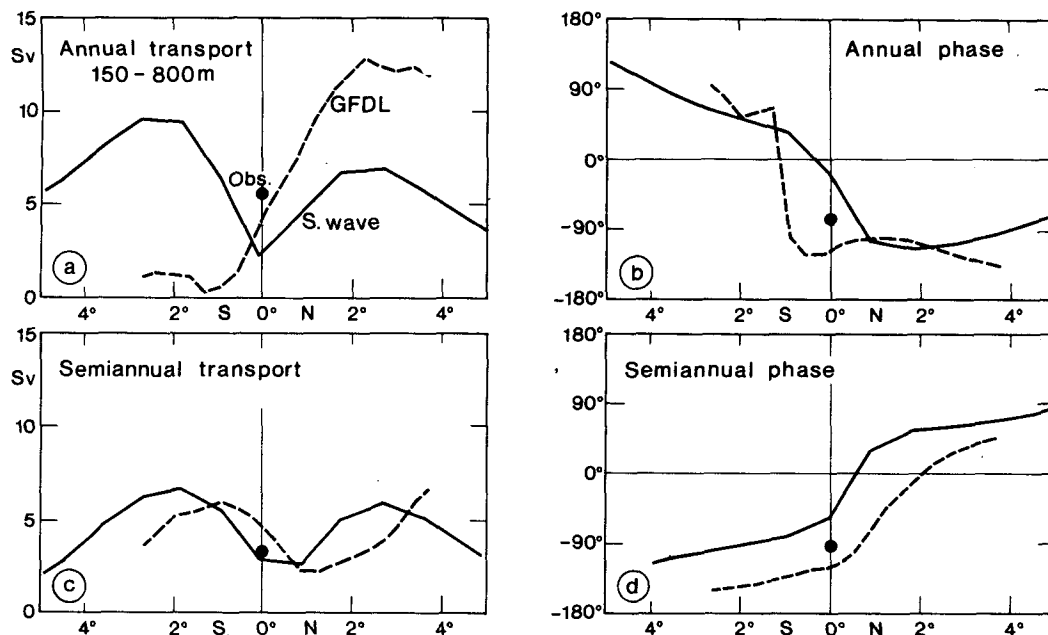
FIG. 14. Western boundary current transport harmonic amplitudes and phases integrated between 150- and 800-m depth for the annual period (a),(b) and semiannual period (c),(d). Solid lines: the short-wave transport (reflected Kelvin wave fit); dashed line: the GFDL model transport (reflected Kelvin wave fit); dashed line: the GFDL model transport, averaged along sections normal to the western boundary of ~2° length; and dot: the averaged observed transport harmonic calculated from all Somali Current moorings at the equator.

alter the observed signal significantly. Nevertheless, Fig. 14 shows the amplitudes and phases of the Somali Current transport between 150- and 800-m depth. The annual GFDL transport variations are at a maximum near 2.5°N with 12 Sv and are small south of the equator. The corresponding short-wave transport is smaller by a factor of 2 north of the equator and larger in the southern part. The semiannual signal is in good agreement between model and waves, with transport variations of maximum 6 Sv if the GFDL model transports are shifted by 1 degree northward (Fig. 14c). The corresponding phase lags by 60°, that is, one month (Fig. 14d). The observed transport variations were estimated by averaging all velocity harmonics for two locations within three vertical boxes located at 43.2° and 43.7°E. The upper layer was centered at 200-m depth with a thickness of 150 m, and the two deeper layers were 250-m thick at 400- and 650-m depth. The horizontal scale (normal to the coastline) was set to be 0.5°, assuming no significant boundary transport east of 44°E, in agreement with the analysis of Schott et al. (1990). The comparison between observations (dots), short-wave, and GFDL model transport variations shows that the observations are not in disagreement with the model analysis, but are located in a region of large meridional changes.

d. Wave fit resolution

The results of the wave fit were examined in terms of resolution and regional dependence by the wave-

model correlation matrix for both periods and the free and reflected Kelvin wave case. It turned out that the Kelvin and Rossby 1 wave were not fully separated and, generally, the first and third baroclinic modes were correlated, but most of the waves were fairly well resolved. This was not the case when only the positions of the Luyten and Roemmich moorings were used.

For the standard case fits the zonal and meridional velocity harmonics were both used. If we only used the zonal velocity, the wave–model correlation got worse for the free Kelvin waves while the resolution of the Rossby plus Kelvin waves for the reflected Kelvin wave fit changed only slightly. Reducing the number of grid points by a factor of 3 drops the resolution drastically, and the energy distributes differently among the waves.

The dependence of the remotely forced western boundary current transport due to the short waves on details of the fit was studied by comparing the standard reflected Kelvin-wave case with the free Kelvin wave case. The individually fitted waves of the free Kelvin wave case fit did not match the western boundary condition. In order to solve the boundary condition, reflected Kelvin waves associated with the individually fitted Rossby waves were used. The resulting annual and semiannual transport amplitudes and phases of the short waves are displayed in Fig. 15 for both reflected (solid) and free (dashed) Kelvin wave fit at 480-m depth. Additionally, the harmonic transport of a reduced Rossby wave set from the standard reflected Kelvin wave fit is included (dotted). For the annual
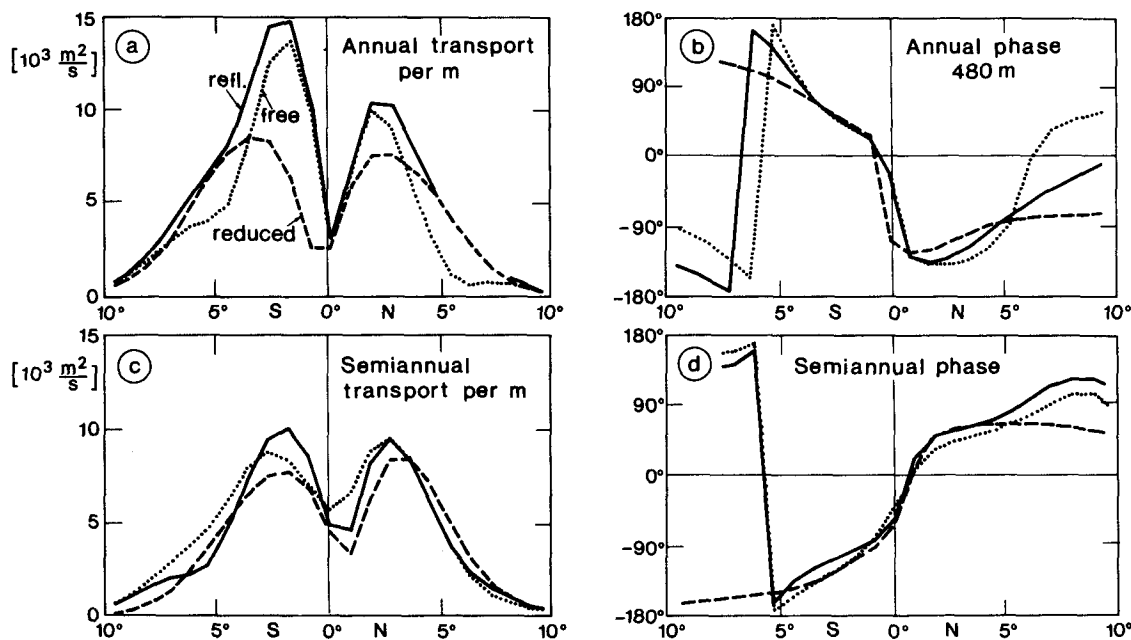
FIG. 15. Short-wave transport (per meter depth) harmonics at 480-m depth for the standard reflected Kelvin wave fit (solid), the free Kelvin wave fit with adapted Kelvin waves (dotted), and a reduced wave set (dashed) (see text for details). The upper panels show the annual amplitude (a) and phase (b) as a function of latitude; the lower panels (c),(d), the semiannual.

period the reduced Rossby wave set contains the first and second baroclinic Rossby 1 wave plus the two reflected Kelvin waves (one for each baroclinic mode). The amplitude in that case is somewhat smaller than for the full set of waves of the other two fits, but the phases compare reasonably well. The semiannual amplitude varies only slightly among the three, and the phases are similar. Here the reduced wave set consists of the first and second baroclinic Rossby 1 and Rossby 2 waves plus the two reflected Kelvin waves. In general, the antisymmetric structure of the short-wave transport at the western boundary turned out to be a robust feature.

5. Summary and conclusions

Seasonal current variations in the western equatorial Indian Ocean of the GFDL model have been analyzed and explained in terms of zonally propagating free equatorial waves for the interior equatorial regime below the thermocline. The aspect of the western boundary current variations being remotely forced by the long waves was then investigated. The physics involved are linear, and seasonal variations consist of annual and semiannual periods.

To justify the use of the GFDL model for the wave analysis we have compared the model with the observed seasonal cycle of equatorial currents and conclude that there exists an overall good qualitative agreement in the upper several 100 m, but there are also some differences.

It is found that the observed zonal ship drift velocities along the equator show mainly semiannual variations (Fig. 4a), while additional annual energy occurs in the model surface currents (Figs. 4b, 7a). Comparing the Hellerman and Rosenstein (1983) wind stress for adjacent grid points at the equator shows mainly semiannual variations for the southern box, 0°–2°S, and annual variations for the wind stress between the equator and 2°N at 55°E (Fig. 2b). Farther east, at 65°E, the semiannual signal is enlarged, but no westward wind stress occurs between May and October in the northern box, and only a weak reversal is seen south of the equator (Fig. 2b). By contrast, FSU ship-observed wind data (J. Legler, personal communication) with one-degree meridional resolution show a significant reversal for the two years analyzed (1987 and 1988) in autumn for the equatorial box at 64°E (not shown). A possible conclusion then is that the coarse (two degree) meridional grid of the Hellerman and Rosenstein (1983) wind-stress fields with no box centered at the equator may be a key to the difference between the observed and model velocities.

The Equatorial Undercurrent is present in the model during the appropriate time of the year in agreement with observations (Fig. 5), but the eastward and upward slant of the core depth, which is typical for the undercurrents of the other oceans, is only found west of 60°E. Below the undercurrent, no vertical variations of zonal currents on small scales (100 m) are present in the model, and the deep flow below 1500 m is weaker than observed along the equator (Fig. 6).

To determine the incident long waves and the associated short-wave boundary transport we had to restrict our wave analysis to the model output fields, since the velocity observations of Luyten and Roemmich were not sufficient to separate different wave modes. The conclusions of the wave fits to the GFDL model velocities are that both fits, the free and reflected Kelvin wave case, represented $\sim$70% of the spatial velocity variance within the GFDL model subregion below the thermocline. But the energy distributed differently among the waves (Fig. 11) depending on whether the Kelvin waves were fitted independently or assumed to be the western-boundary reflected Rossby waves. It turned out that some of the waves were linearly dependent (e.g., Kelvin and Rossby 1 wave for the free Kelvin wave case), which might explain part of the difference between the free and reflected Kelvin wave fit energy. Generally, the more energetic long waves were of a symmetrical meridional mode. At the western boundary this results in an antisymmetrical meridional structure of the short-wave transport in order to balance the flux, normal to the western boundary, between incoming symmetrical Rossby waves and reflected Kelvin waves (Cane and Gent 1984).

A comparison for the semiannual velocity harmonics of the observations (Luyten and Roemmich 1982), the model of Gent et al. (1983), the GFDL model, and both fits to the GFDL model is given by Table 1. While model results show a westward and upward phase propagation throughout the array, the observations indicate eastward phase propagation west of 58°E in the 200-m layer and that the observed amplitudes in the deeper layers are larger than those from the models. One reason for both of these differences may again be the deficiency of the particular climatological wind stress applied to the models. The comparison of the harmonics at individual points can be summarized by the spatial correlation between the five datasets over the 11 mooring locations (Table 3). For the semiannual period (upper right part) the GFDL model harmonics explain 66% of the observed spatial variance, and the wave fits to the model (with 68% and 70%) are closer to the observations than the wave model of Gent

TABLE 3. Resolved spatial variance in percent of the annual (lower left) and semiannual (upper right) harmonic zonal velocity of the 11 mooring locations of Table 1.

Resolved spatial variance of the harmonics (%)

	Waves reflected	GFDL model	L and R observation	Gent et al. (1983) wave model
				semiannual
Free waves	—	93	70	84
Reflected waves	—	94	68	76
GFDL	95	—	66	76
L and R	45	58	—	44
	annual			

et al. (1983). The annual harmonics of the GFDL model and wave fit compare less well to the observations ($\sim$50%).

Our main finding is the antisymmetrical structure of the short-wave–induced western boundary current transport with respect to the equator. The short waves were determined by the western boundary condition of reflected long equatorial waves, which were fitted to the GFDL model velocities in a subthermocline region.

Conclusions from the western boundary current analysis are that part of the subthermocline GFDL model variations were found to be consistent with the remotely forced short-wave transport. The antisymmetrical transport variation with respect to the equator was seen between February and September (Fig. 13) for both the short waves and the GFDL model fields, and compared better for the semiannual than the annual period (Fig. 14). The Somali Current moorings located directly on the equator helped less than anticipated to determine the effect of remote forcing from the interior since they were close to the node of the antisymmetrical meridional variations. But nevertheless, amplitudes and phases of the observed boundary current variations were not in disagreement with the short-wave–induced transport. Other observational evidence is found in Leetmaa et al. (1982), where the observed Somali Current velocities in June show an antisymmetric structure with northeastward flow at 3°N and southwestward flow at 2°S at the 700-m level, in qualitative agreement with the remotely forced short-wave transport for June (Fig. 13a). Sensitivity studies of the wave fit to changes in model data used or wave modes fitted suggest that the antisymmetrical short-wave transport at the western boundary is a robust feature.

We cannot claim to have proven the existence of long equatorial waves remotely forcing the subthermocline Somali Current variations in the real ocean, but the analysis of the GFDL model suggests that the short-wave transport plays an important role in understanding the current variations at the western boundary below the thermocline.

APPENDIX

Equatorial Waves

a. Equatorial dispersion relation

Following Lighthill (1969) and Moore and Philander (1977), the linear inviscid equatorial beta-plane equa-

tions were used and the vertical problem was separated by normal vertical modes. For wave-type solutions in the x direction: $u, v, p \sim e^{i(Kx-\omega t)}$, the resulting dispersion relation is given by

$$K_{\pm} = -\frac{1}{2\omega} \mp \left[\omega^2 + \frac{1}{4\omega^2} - (2m+1)\right]^{1/2}, \quad \text{(A1)}$$

and the wave velocities are the real part of

Rossby wave ($m \geq 1$):

$$u_m = i\left[\frac{\sqrt{m/2}}{(\omega + K_{\pm})} \cdot \psi_{m-1} + \frac{\sqrt{(m+1)/2}}{(\omega - K_{\pm})} \cdot \psi_{m+1}\right]$$
$$\times e^{i(K_{\pm}x-\omega t)},$$

$$v_m = \psi_m e^{i(K_{\pm}x-\omega t)},$$

$$p_m = i\left[\frac{\sqrt{m/2}}{(\omega + K_{\pm})} \cdot \psi_{m-1} - \frac{\sqrt{(m+1)/2}}{(\omega - K_{\pm})} \cdot \psi_{m+1}\right]$$
$$\times e^{i(K_{\pm}x-\omega t)}; \quad \text{(A2)}$$

Yanai wave ($m = 0$):

$$u = p = i\frac{\omega}{\sqrt{2}}\psi_1 e^{i(K_+ x-\omega t)},$$

$$v = \psi_0 \cdot e^{i(K_+ x-\omega t)};$$

with

$$K_+ = K_0 = \omega - \frac{1}{\omega}; \quad \text{and} \quad \text{(A3)}$$

Kelvin wave ($m = -1$):

$$u = p = i\psi_0 e^{i(K_+ x-\omega t)},$$

$$v = 0;$$

with

$$K_+ = K_{-1} = \omega. \quad \text{(A4)}$$

Here $K_{\pm}$ indicates eastward (+) or westward (−) group velocity, and the meridional dependence $\psi_m(y)$ is given by

$$\psi_m = \frac{e^{-y^2/2}H_m(y)}{\sqrt{2^m m!}\sqrt{\pi}},$$

with H_m denoting the mth Hermite polynomial.

At the periods considered here, only Kelvin and long Rossby waves exist in the interior equatorial ocean. Their energies are

$$E_{Kel} = \frac{|A|^2}{2},$$

$$E_R = \frac{|A|^2}{4}\left[1 + \frac{m+1}{(\omega - K)^2} + \frac{m}{(\omega + K)^2}\right], \quad \text{(A5)}$$

where A denotes the wave amplitude.

b. Wave reflection at an inclined western boundary

Let Θ be the angle that the coastline makes with north, $\mathbf{u}$ the horizontal velocity vector, $\mathbf{n}$ a unit vector normal to the straight coastline, and define $\gamma = \tan\Theta$. Following Cane and Gent (1984), the boundary condition $\mathbf{u} \cdot \mathbf{n} = 0$ leads to the principle that the amplitude A_K of the reflected Kelvin wave may be calculated in terms of the incident long Rossby waves without considering the short Rossby waves at all using the mass flux normal to the coastline:

$$U = \int_{-\infty}^{+\infty} [u(y) - \gamma v(y)]e^{iK_{rr}y}dy. \quad \text{(A6)}$$

A little algebra leads to the flux for each wavemode:

$$U_K = i\sqrt{2\pi}\psi_0(K\gamma), \quad \text{(A7)}$$

$$U_R = i^{(m-1)}\sqrt{2\pi}[p_m(K\gamma) - i\gamma\psi_m(K\gamma)]. \quad \text{(A8)}$$

The normal boundary condition applied to the normal fluxes leads to the Kelvin wave amplitude for an incoming long Rossby wave of unit amplitude:

$$A_K = \frac{-U_R}{U_K} = i^{(m)}\frac{[p_m(K\gamma) - i\gamma\psi_m(K\gamma)]}{\psi_0(K\gamma)}. \quad \text{(A9)}$$

c. Western boundary short-wave transport

The alongshore western boundary current transport is formed by the sum of all short Rossby and Yanai waves, which are trapped at the western boundary because their group velocity is so small $[O(\omega^2)]$ (Cane and Gent 1984). Each of these waves satisfies the dispersion relation from (1) and (3):

$$K = -\frac{1}{\omega} + O(\omega).$$

And each is nondivergent to $O(\omega^2)$, so there exists a streamfunction

$$\phi(n, s, t) = \tilde{\phi}(s)e^{i(-n/\omega-\omega t)},$$

where s is the along-coastline direction such that

$$\mathbf{u}^B = \mathbf{k} \times \nabla\phi,$$

where $\mathbf{u}^B$ is the velocity of the sum of these short waves and $\mathbf{k}$ an upward unit vector.

The streamfunction is determined numerically by integrating the no-normal flow boundary condition along the coastline,

$$\frac{\delta\tilde{\phi}}{\delta s} = -\mathbf{u}^B \cdot \mathbf{n} = (v\cos\Theta - u\sin\Theta)_{R+K}, \quad \text{(A10)}$$

with the boundary condition being $\phi(\pm\infty) = 0$, where the subscript $R + K$ denotes the combined long Rossby and Kelvin wave contributions.

d. Wave fit

The horizontal velocities were transformed in Fourier space by harmonic analysis giving complex velocities $U(x, y, z)$ and $V(x, y, z)$, represented by the data vector $\mathbf{d}$. The wave matrix $\mathbf{W}$ contains a row vector of complex velocities u_{Rnm} or v_{Rnm} for each location $(x,$ $y, z)$ and a column for each wave (unit amplitude and zero phase) with respect to meridional m and vertical n modes. In the reflected Kelvin wave fit the velocity of the appropriate western boundary reflected Kelvin u_{Knm} wave (see Appendix, section b) is added; otherwise, the Kelvin waves will show explicitly. The result is the complex wave amplitude vector $\mathbf{a}$. The reflected Kelvin wave problem is described by

$$
\begin{bmatrix} U_a \\ V_a \\ \vdots \\ U_b \\ \vdots \end{bmatrix} = \begin{bmatrix} u_{aR11} + u_{aK11} & u_{aR12} + u_{aK12} & & u_{aR21} + u_{aK21} & \\ v_{aR11} & v_{aR12} & & v_{aR21} & \\ & & \ddots & & \\ u_{bR11} + u_{bK11} & u_{bR12} + u_{bK12} & & u_{bR21} + u_{bK21} & \\ & & & & \ddots \end{bmatrix} \cdot \begin{bmatrix} a_{R11} \\ a_{R12} \\ \vdots \\ a_{R21} \\ \vdots \end{bmatrix},
$$

or more generally

$$\mathbf{d} = \mathbf{Wa}, \tag{A11}$$

with the least-squares solution,

$$\mathbf{a} = [\mathbf{W}^T\mathbf{W}]^{-1}\mathbf{W}^T\mathbf{d}, \tag{A12}$$

being solved separately for the annual and semiannual waves.

REFERENCES

Cane, M. A., and E. S. Sarachik, 1977: Forced baroclinic ocean motions. II. The linear equatorial bounded case. *J. Mar. Res.,* **35,** 395–432.
——, and P. R. Gent, 1984: Reflection of low-frequency equatorial waves at arbitrary western boundaries. *J. Mar. Res.,* **42,** 487–502.
Cutler, A., and J. Swallow, 1984: Surface currents of the Indian Ocean (to 25°S, 100°E): Compiled from historical data archieved by the Meteorological Office, Bracknell, U.K. Institute of Oceanographical Science, Rep. No. 1987, 8 pp. and 36 charts.
Düing, W., and F. Schott, 1978: Measurements in the source region of the Somali Current during the monsoon reversal. *J. Phys. Oceanogr.,* **8,** 278–289.
Gent, P. R., K. O'Neill, and M. A. Cane, 1983: A model of the semiannual oscillation in the equatorial Indian Ocean. *J. Phys. Oceanogr.,* **13,** 2148–2160.
Hellerman, S., and M. Rosenstein, 1983: Normal monthly wind stress over the World Ocean with error estimates. *J. Phys. Oceanogr.,* **13,** 1093–1104.
Leetmaa, A., and H. Stommel, 1980: Equatorial current observations in the western Indian Ocean in 1975 and 1976. *J. Phys. Oceanogr.,* **10,** 258–269.
——, D. R. Quadfasel, and D. Wilson, 1982: Development of the flow field during the onset of the Somali Current, 1979. *J. Phys. Oceanogr.,* **12,** 1325–1342.

Lighthill, M. J., 1969: Dynamic response of the Indian Ocean to onset of the southwest monsoon. *Phil. Trans. Roy. Soc. London,* **A265,** 45–92.
Luyten, J. R., and J. C. Swallow, 1976: Equatorial undercurrents. *Deep-Sea Res.,* **23,** 999–1001.
——, and D. H. Roemmich, 1982: Equatorial currents at semi-annual period in the Indian Ocean. *J. Phys. Oceanogr.,* **12,** 406–413.
Moore, D., and G. Philander, 1977: Modelling of the tropical oceanic circulation. *The Sea, Marine Modeling,* Vol. 6, E. D. Goldberg, I. N. McCave, J. J. O'Brian, and J. H. Steele, Eds., Wiley-Interscience, 319–361.
Philander, S. H., and R. C. Pacanowski, 1986: A model of the seasonal cycle in the tropical Atlantic Ocean. *J. Geophys. Res.,* **91,** 14 192–14 206.
Ponte, R. M., and J. R. Luyten, 1990: Deep velocity measurements in the western equatorial Indian Ocean. *J. Phys. Oceanogr.,* **20,** 44–52.
Reverdin, G., 1987: The upper equatorial Indian Ocean: The climatological seasonal cycle. *J. Phys. Oceanogr.,* **17,** 903–927.
Schott, F., 1986: Seasonal variation of cross-equatorial flow in the Somali Current. *J. Geophys. Res.,* **91,** 10 581–10 584.
——, J. Swallow, and M. Fieux, 1990: The Somali Current at the equator: Annual cycle of currents and transports in the upper 1000 m and connections to neighbouring latitudes. *Deep-Sea Res.,* **37,** 1825–1848.
——, M. Fieux, J. Kindle, J. Swallow, and R. Zantopp, 1988: The boundary currents east and north of Madagascar. 2: Direct measurements and model comparisons. *J. Geophys. Res.,* **93,** 4963–4974.
Taft, B. A., and J. A. Knauss, 1967: The Equatorial undercurrent of the Indian Ocean as observed by the LUSIAD Expedition. *Bull. Scripps Inst. Oceanogr.,* **9,** 163 pp.
Veronis, G., 1965: On parametric values and types of representation in wind-driven ocean circulation studies. *Tellus,* **14,** 77–84.
Wunsch, C., 1977: Response of an equatorial ocean to a periodic monsoon. *J. Phys. Oceanogr.,* **7,** 497–511.
Wyrtki, K., 1973: An equatorial jet in the Indian Ocean. *Science,* **181,** 262–264.